Scilight

Regenerative Medicine and Dentistry
https://www.sciltp.com/journals/rmd



Article

Micro/Nano Bioactive Glass Spheres Produced by Extended Synthesis Are Associated with Attenuated Inflammatory Responses and Enhanced Reparative Dentin Formation

Zhengmao Li [1], Tao Wang [2], Yin Xiao [1,3] and Yinghong Zhou [4,5,*]

[1] School and Hospital of Stomatology, Guangdong Engineering Research Center of Oral Restoration and Reconstruction, Guangzhou Key Laboratory of Basic and Applied Research of Oral Regenerative Medicine, Guangzhou Medical University, Guangzhou 510182, China
[2] GemPharmatech Co., Ltd., Guangzhou 528000, China
[3] School of Medicine and Dentistry, Griffith University, Gold Coast, QLD 4222, Australia
[4] School of Dentistry, The University of Queensland, Brisbane, QLD 4006, Australia
[5] Centre for Orofacial Regeneration, Reconstruction, and Rehabilitation (COR3), The University of Queensland, Brisbane, QLD 4006, Australia
* Correspondence: yinghong.zhou@uq.edu.au

How To Cite: Li, Z.; Wang, T.; Xiao, Y.; et al. Micro/Nano Bioactive Glass Spheres Produced by Extended Synthesis Are Associated with Attenuated Inflammatory Responses and Enhanced Reparative Dentin Formation. *Regenerative Medicine and Dentistry* **2026**, *3*(4), 18. https://doi.org/10.53941/rmd.2026.100018

Received: 24 August 2026
Revised: 20 October 2026
Accepted: 16 November 2026
Published: 26 November 2026

Abstract: Effective vital pulp therapy requires biomaterials that modulate inflammation while supporting reparative dentin formation. Micro/nano bioactive glass (MNBG) spheres promote mineralization through their surface reactivity and ionic dissolution products, but the influence of particle topography on their immunomodulatory and dentinogenic properties remains incompletely understood. Here, rough-surfaced MNBG spheres (MNBGr) were produced by extending the synthesis time and compared with conventional MNBG spheres. Their physicochemical characteristics and biological performance were evaluated using RAW 264.7 macrophages, primary human dental pulp cells (DPCs), and a rat direct pulp capping model. Compared with MNBG, MNBGr reduced lipopolysaccharide-induced pro-inflammatory gene expression in macrophages and enhanced alkaline phosphatase activity, mineralized matrix deposition, and mineralization-associated gene expression in DPCs. At 2 weeks after direct pulp capping, MNBGr-treated teeth exhibited radiopaque mineralized tissue and increased collagen deposition relative to untreated controls, together with higher Arg1 immunostaining. Collectively, these findings associate the extended-synthesis MNBGr formulation with attenuated inflammatory responses, enhanced DPC mineralization, and early reparative dentin formation, supporting its further development as a multifunctional biomaterial for vital pulp therapy.

Keywords: bioactive glass; surface topography; immunomodulation; reparative dentin; direct pulp capping

1. Introduction

Dental caries is a biofilm-mediated, sugar-driven disease characterized by dynamic cycles of demineralization and remineralization within dental hard tissues [1]. When a carious lesion extends into dentin and approaches or exposes the dental pulp, its management becomes a biological as well as a restorative challenge. Treatment should control infection and restore lost tooth structure while, where clinically feasible, preserving pulp

Copyright: © 2026 by the authors. This is an open access article under the terms and conditions of the Creative Commons Attribution (CC BY) license (https://creativecommons.org/licenses/by/4.0/).
Publisher's Note: Scilight stays neutral with regard to jurisdictional claims in published maps and institutional affiliations.

vitality and promoting the formation of a protective mineralized barrier [2]. These outcomes depend on the capacity of the dentin-pulp complex to regulate inflammation, maintain viable reparative cells, deposit extracellular matrix, and initiate reparative dentin formation [3]. Biomaterials intended for vital pulp therapy should therefore support hard tissue formation while maintaining an immune microenvironment compatible with tissue healing.

Micro/nano bioactive glasses (MNBGs) offer a promising strategy for addressing these requirements. Their reactive surfaces undergo ion exchange and dissolution, creating conditions that favor apatite nucleation and mineralized-matrix deposition [4]. The resulting ionic products may also support angiogenesis, wound healing, antibacterial activity, and cellular processes involved in tissue repair [5,6]. Because pulp healing requires both mineralization and appropriate control of inflammation, the biological performance of MNBGs depends on more than chemical composition alone. Physical properties that govern interactions with proteins, cells, and tissues are also likely to shape the reparative response [7].

Surface architecture is particularly relevant because micro/nanoscale topographical features can influence protein adsorption, cell adhesion, cytoskeletal organization, phagocytic interactions, and downstream signaling [8]. These features may also increase the reactive area available for ion exchange and apatite nucleation, thereby linking cell regulatory activity with mineralization. Macrophages are key mediators at this biomaterial-tissue interface, as they sense physicochemical cues and coordinate inflammatory and reparative responses through cytokine production, redox and iron homeostasis, extracellular matrix remodeling, and communication with resident progenitor cells [9]. Dental pulp cells (DPCs), in turn, contribute directly to reparative matrix deposition and mineralization after injury [10]. Our previous work with Ca-Zn-Si micro/nano spheres showed that biomaterial-mediated regulation of macrophage responses can be accompanied by enhanced DPC mineralization [11], supporting an osteoimmune approach to pulp-capping material design. Surface topography represents an additional design parameter through which these complementary responses may be optimized.

In the present study, we compared rough-surfaced micro/nano bioactive glass spheres (MNBGr), produced by extending the synthesis time, with conventional MNBG spheres. We hypothesized that the extended-synthesis formulation would attenuate pro-inflammatory macrophage signaling, enhance mineralization-associated responses in primary human DPCs, and support early reparative dentin formation. The two formulations were characterized physicochemically and evaluated in RAW 264.7 macrophages, primary human DPCs, and a rat direct pulp-capping model. This integrated assessment examined the inflammatory and mineralization-associated responses relevant to the development of bioactive materials for vital pulp therapy.

2. Materials and Methods

2.1. Synthesis of MNBG and MNBGr Spheres

MNBG and MNBGr spheres were synthesized through the hydrolysis of tetraethyl orthosilicate (TEOS, 98%) using ammonium hydroxide (NH_4OH, 99%) as the catalyst. Ethanol (60 mL), deionized water (6 mL), and NH_4OH (15 mL) were mixed and stirred for 20 min. TEOS (6 mL) was then added, and the mixture was stirred for a further 30 min. Calcium nitrate tetrahydrate ($Ca(NO_3)_2 \cdot 4H_2O$, 99%; 9.0 g) was added, after which the suspensions were stirred for 2 h to obtain MNBG or for 24 h to obtain MNBGr. The precipitates were collected by centrifugation, washed twice with ethanol, precooled in water, vacuum-dried at −30 °C for 48 h, and calcined at 650 °C for 1 h.

2.2. Physicochemical Characterization of MNBG and MNBGr Spheres

Crystal structure was examined by X-ray diffraction (XRD; X'Pert PRO, PANalytical, Almelo, The Netherlands) using Cu Kα radiation (λ = 0.15418 nm). Particle morphology was assessed by transmission electron microscopy (TEM; JEM-1400, JEOL, Tokyo, Japan) at 100 kV and field-emission scanning electron microscopy (FESEM; JSM-7100, JEOL, Tokyo, Japan) at 5 or 10 kV. Elemental composition was analyzed by energy-dispersive X-ray spectroscopy. Particle-size distribution and zeta potential were measured using a Zetasizer Nano ZS (Malvern Instruments, Worcestershire, UK), and Fourier-transform infrared spectra were acquired with a Nicolet iS50 spectrometer over 2000–400 cm^{-1}.

2.3. RAW 264.7 Cell Culture and Isolation of Primary Human Dental Pulp Cells

RAW 264.7 murine macrophage-like cells (Procell Life Science & Technology Co., Ltd., Wuhan, China) were maintained in Dulbecco's modified Eagle medium (DMEM) supplemented with 10% fetal bovine serum and 100 U/mL penicillin-streptomycin. The medium was replaced every 2 days, and cells were passaged at approximately 80% confluence.

Impacted third molars were collected from healthy adult donors (n = 6; 18–30 years of age) after written informed consent and approval by the Human Research Ethics Committee of the Affiliated Stomatology Hospital of Guangzhou Medical University (JCYJ2024004). Pulp tissue was removed aseptically, minced, washed with phosphate-buffered saline (PBS), and cultured by explant outgrowth in DMEM containing 10% fetal bovine serum and 1% penicillin-streptomycin at 37 °C in 5% CO_2. Primary DPCs were passaged at approximately 80% confluence.

2.4. CCK-8 Metabolic Activity Assay

RAW 264.7 cells were seeded in 96-well plates at 2×10^3 cells per well and exposed to the indicated concentrations of MNBG or MNBGr for 24 h. CCK-8 reagent (10 μL; Dojindo, Kumamoto, Japan) in 100 μL of culture medium was added to each well and incubated at 37 °C for 2 h. Absorbance at 450 nm was measured using a microplate reader (Molecular Devices, LLC, San Jose, CA, USA).

2.5. Cell-Associated Particles

RAW 264.7 cells were seeded in 24-well plates at 2×10^4 cells per well and incubated overnight. The medium was then replaced with complete medium containing FITC-labeled MNBG or MNBGr (100 μg/mL). After 6 h, the cells were washed twice with PBS and fixed with 4% (*w*/*v*) paraformaldehyde for 30 min at room temperature.

F-actin was labeled with TRITC-phalloidin, and nuclei were counterstained with DAPI. Images were acquired by confocal laser-scanning microscopy (A1R, Nikon, Tokyo, Japan), and cell-associated fluorescent particles were assessed qualitatively.

2.6. RNA Extraction and Reverse-Transcription Quantitative PCR

RAW 264.7 cells were stimulated with lipopolysaccharide (LPS; 100 ng/mL) and then treated with MNBG or MNBGr (100 μg/mL) for 24 h. For mineralization-associated gene-expression analysis, DPCs were exposed to MNBG or MNBGr (100 μg/mL) for 3 days. Total RNA was extracted using TRIzol reagent (Life Technologies Pty Ltd., Melbourne, VIC, Australia). RNA concentration and purity were assessed using a NanoDrop 1000C spectrophotometer (Thermo Fisher Scientific, Waltham, MA, USA), and cDNA was synthesized with a commercial kit (Bioline Australia Pty Ltd., Sydney, NSW, Australia) according to the manufacturer's instructions.

RT-qPCR was performed using a QuantStudio 7 Flex Real-Time PCR System (Thermo Fisher Scientific). Relative gene expression was normalized to *Gapdh* in mouse cells or *ACTB* in human DPCs and calculated using the $2^{-\Delta\Delta Cq}$ method. Primers were synthesized by Sangon Biotech (Shanghai, China), and their sequences are listed in Table 1.

Table 1. Primer sequences used for RT-qPCR.

Target Gene	Primer Sequence (5′-3′)
Mouse (*Mus musculus*)	
Gapdh	Forward: 5′-GTGTCCGTCGTGGATCTGA-3′ Reverse: 5′-CCTGCTTCACCACCTTCTTG-3′
Il1b	Forward: 5′-TGGAGAGTGTGGATCCCAAG-3′ Reverse: 5′-GGTGCTGATGTACCAGTTGG-3′
Il6	Forward: 5′-CACAGAGGATACCACTCCCAACA-3′ Reverse: 5′-TCAGAATTGCCATTGCACAAC-3′
Tnf	Forward: 5′-CTGAACTTCGGGGTGATCGG-3′ Reverse: 5′-GGCTTGTCACTCGAATTTTGAGA-3′
Nos2	Forward: 5′-CAGAAGTGCAAAGTCTCAGACAT-3′ Reverse: 5′-GTCATCTTGTATTGTTGGGCT-3′
Human (*Homo sapiens*)	
ACTB	Forward: 5′-TCCAGCTCCTCCCTGGAG-3′ Reverse: 5′-ACAGGACTCCATGCCCAG-3′
OPN	Forward: 5′-TCACCAGTCTGATGAGTCTCACCATTC-3′ Reverse: 5′-TAGCATCAGGGTACTGGATGTCAGGTC-3′

Table 1. *Cont.*

Target Gene	Primer Sequence (5′-3′)
Human (*Homo sapiens*)	
RUNX2	Forward: 5′-CATGGCGGGTAACGATGAA-3′ Reverse: 5′-AGACGGTTATGGTCAAGGTGAAA-3′
COL1A2	Forward: 5′-GCAACATGCCAATCTTTACAAGAG-3′ Reverse: 5′-CCATCATACTGAGCAGCAAAGTTC-3′

2.7. Alkaline Phosphatase Activity and Alizarin Red S Staining

DPCs were seeded in 24-well plates at 2×10^4 cells per well and cultured with the indicated material treatment. On day 7, alkaline phosphatase (ALP) activity was quantified by p-nitrophenyl phosphate conversion and normalized to total protein measured using a bicinchoninic acid assay (Beyotime Institute of Biotechnology, Shanghai, China). Results were expressed as p-nitrophenol equivalents.

For mineral-deposition analysis, DPCs were cultured for 14 days, washed twice with PBS, fixed with 4% paraformaldehyde for 15 min, and stained with 40 mM Alizarin Red S for 30 min at room temperature. Excess stain was removed with distilled water, and the plates were air-dried before imaging by optical microscopy.

For quantification, bound dye was extracted with 300 μL of 50% acetic acid for 10 min. The extract was transferred to a 1.5-mL tube, vortexed for 30 s, neutralized with 650 μL of 4 mol/L NaOH, and centrifuged. Aliquots of supernatant (100 μL, in technical triplicate) were transferred to a 96-well plate, and absorbance was measured at 405 nm.

2.8. Rat Direct Pulp-Capping Model

All animal procedures were approved by the Animal Ethics Committee of Guangzhou Medical University (20191115006) and conducted in accordance with the committee's animal welfare requirements. The study was reported in accordance with the ARRIVE guidelines. Nine male Sprague-Dawley rats (200–250 g) were anesthetized by intraperitoneal injection of phenobarbital sodium (30 mg/kg). A cavity was prepared on the mesial surface of the maxillary first molar using a no. 1/4 round bur, and the pulp was exposed with a DG16 explorer. Exposure was confirmed by minor bleeding. The cavity was rinsed with sterile saline, and the pulp surface was gently dried with a sterile cotton pellet.

Animals were allocated to control, MNBG, and MNBGr groups (n = 3 animals per group). For the material-treated groups, 30 mg of MNBG or MNBGr powder was mixed with PBS and applied to the exposure site; exposed pulps in the control group received no bioactive glass. Animals were euthanized 2 weeks after surgery. Treated teeth were harvested, fixed in 4% paraformaldehyde, and scanned using a SkyScan 1172 micro-computed tomography (micro-CT) system (Bruker, Kontich, Belgium) at 60 kV with a 0.5-mm aluminum filter. Images were reconstructed using NRecon and visualized using CTvox and CTAn software (Bruker, Kontich, Belgium).

2.9. Histology and Immunohistochemistry

After micro-CT imaging, teeth were decalcified in 10% ethylenediaminetetraacetic acid at room temperature for 4 weeks with weekly solution changes. Samples were dehydrated through graded ethanol, cleared in xylene, embedded in paraffin, and sectioned at 5 μm. Sections were stained with hematoxylin and eosin or Masson's trichrome. Immunohistochemistry was performed for inducible nitric oxide synthase (iNOS) and arginase-1 (Arg1).

For quantitative analysis of collagen deposition and iNOS and Arg1 immunostaining, tissue sections were imaged at ×20 magnification. Within the defect region, stain-positive areas were segmented using color deconvolution in ImageJ/Fiji. The positive area was expressed as a percentage of the total tissue area within the region of interest.

2.10. Statistical Analysis

Statistical analyses were performed using GraphPad Prism 8.0 (GraphPad Software, San Diego, CA, USA). Data are presented as mean ± standard deviation (SD). Unpaired two-tailed t tests were used for comparisons between two groups. Comparisons involving three or more groups were performed using one-way analysis of variance (ANOVA) followed by Tukey's multiple-comparisons test. Normality and homogeneity of variance were assessed using the Shapiro-Wilk and Levene tests, respectively. All tests were two-sided, and $p < 0.05$ was considered statistically significant.

3. Results

3.1. Physicochemical Characterization of MNBG and MNBGr Spheres

MNBG and MNBGr spheres were synthesized using a modified Stöber process. SEM and TEM showed spherical particles in both groups. MNBG displayed a comparatively smooth surface, whereas MNBGr exhibited a distinctive rough surface composed of flake-like features (Figure 1A,B). Thus, extending the synthesis time produced a clear change in particle surface architecture.

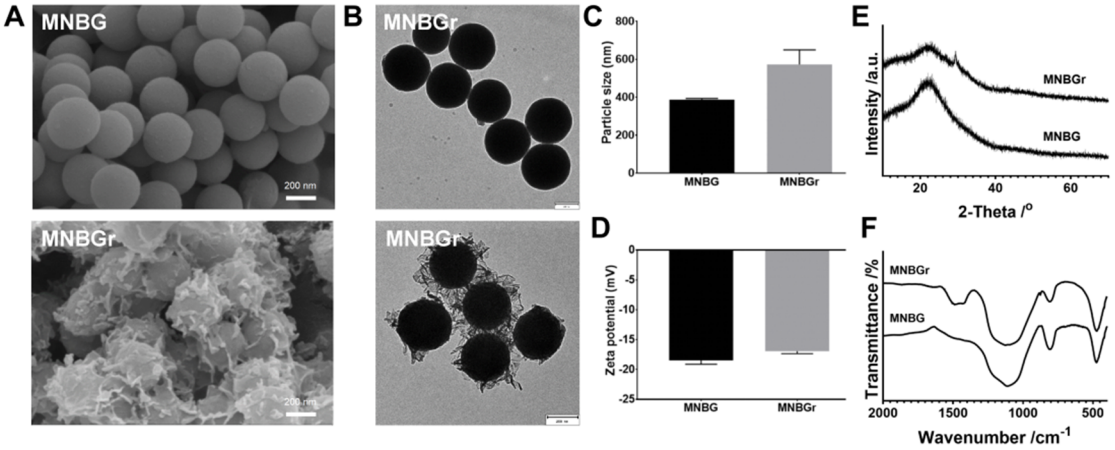

Figure 1. Physicochemical characterization of micro/nano bioactive glass spheres. (**A**) SEM images showing the comparatively smooth surface of MNBG and the rough, flake-like surface of MNBGr. (**B**) TEM images of particle morphology (scale bar, 200 nm). (**C**) Particle-size distribution. (**D**) Zeta potential. (**E**) XRD patterns showing the amorphous structure of both formulations. (**F**) FTIR spectra showing characteristic silicate-network bands.

Energy-dispersive X-ray spectroscopy confirmed the elemental composition of both formulations. The mean particle diameter was 387.2 ± 6.3 nm for MNBG and 572.6 ± 76.9 nm for MNBGr (Figure 1C), indicating that the extended synthesis also increased particle size. Zeta-potential measurements are shown in Figure 1D. Both materials produced a broad XRD halo characteristic of an amorphous glass structure (Figure 1E). FTIR bands at approximately 794 and 1079 cm^{-1} were assigned to Si-O bending and asymmetric Si-O-Si stretching vibrations, respectively (Figure 1F) [12].

3.2. Effects of MNBG and MNBGr on Inflammatory Markers In Vitro

RAW 264.7 cells remained adherent and displayed a well-spread morphology after 24 h of exposure to MNBG or MNBGr, indicating good short-term cell compatibility (Figure 2A).

Confocal microscopy showed FITC-labeled MNBG and MNBGr associated with RAW 264.7 cells after 6 h (Figure 2B). Fluorescent particles were observed associated with the projected cell boundaries, consistent with active macrophage-particle interactions.

Neither material reduced CCK-8 metabolic activity after 24 h across the tested concentration range (Figure 2C). Increased absorbance was observed at 50 and 100 μg/mL for MNBG and at several MNBGr concentrations. Based on these responses, 100 μg/mL was selected for subsequent experiments.

Following LPS stimulation, both MNBG and MNBGr reduced the expression of the pro-inflammatory genes *Il1b*, *Il6*, *Tnf*, and *Nos2* relative to the LPS group (Figure 2D). The reductions were greater in the MNBGr group than in the MNBG group under the conditions examined, associating the extended-synthesis formulation with stronger attenuation of LPS-induced inflammatory gene expression in RAW 264.7 cells.

3.3. Effects of MNBG and MNBGr on DPC Mineralization-Associated Responses

DPCs in all groups remained adherent and well spread after 24 h, with particles visible on or near cells in the material-treated groups (Figure 3A). After 14 days, MNBGr produced the most extensive Alizarin Red S staining, and dye extraction confirmed significantly greater mineralized-matrix deposition than in the control and MNBG groups (Figure 3B,C). MNBGr also increased ALP activity at day 7 (Figure 3D). At day 3, expression of *OPN*, *RUNX2*, and *COL1A2* was higher in the MNBGr group than in the untreated control, although the magnitude of the response varied among genes (Figure 3E). Together, these results associate MNBGr with enhanced mineralization-related activity and mineralized matrix formation in primary human DPCs.

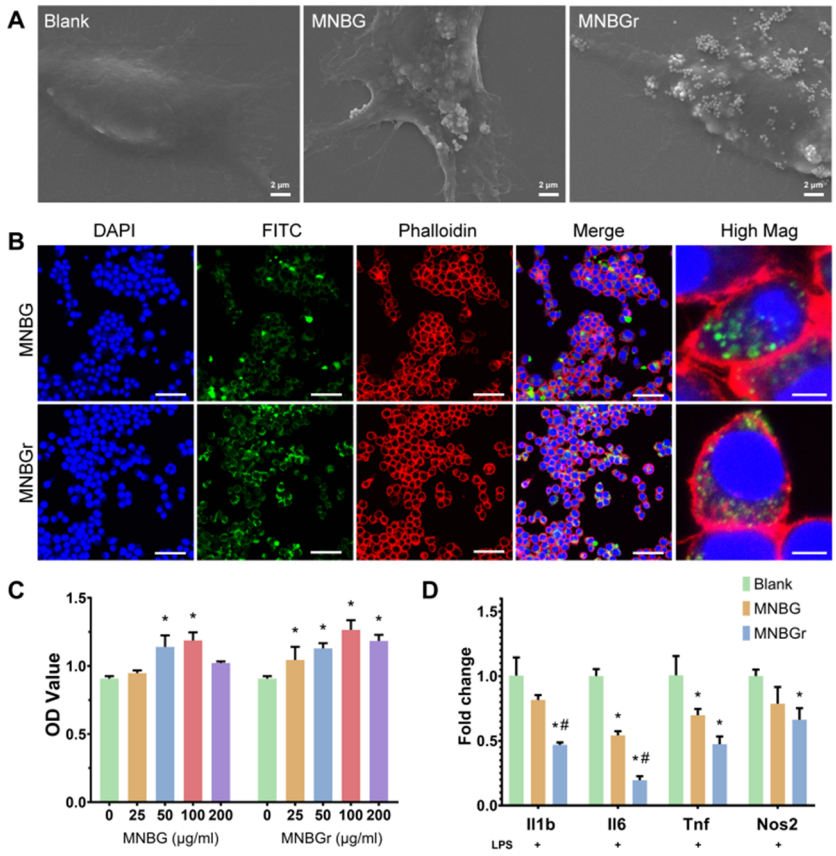

Figure 2. Association of MNBG and MNBGr with RAW 264.7 cells and effects on inflammatory gene expression. (**A**) SEM images after 24 h of material exposure. (**B**) Confocal images of RAW 264.7 cells exposed to FITC-labeled MNBG or MNBGr; nuclei are shown in blue (DAPI), particles in green (FITC), and F-actin in red (TRITC-phalloidin). Scale bars, 50 μm (low magnification) and 5 μm (high magnification). The images demonstrate cell-associated fluorescence but do not distinguish internalized from surface-bound particles. (**C**) CCK-8 metabolic activity after 24 h of exposure to the indicated particle concentrations. (**D**) Relative *Il1b*, *Il6*, *Tnf*, and *Nos2* mRNA expression after 24 h of LPS stimulation and material treatment. Data are presented as mean ± SD from three independent experiments. * $p < 0.05$ versus the control group; # $p < 0.05$ versus the MNBG group.

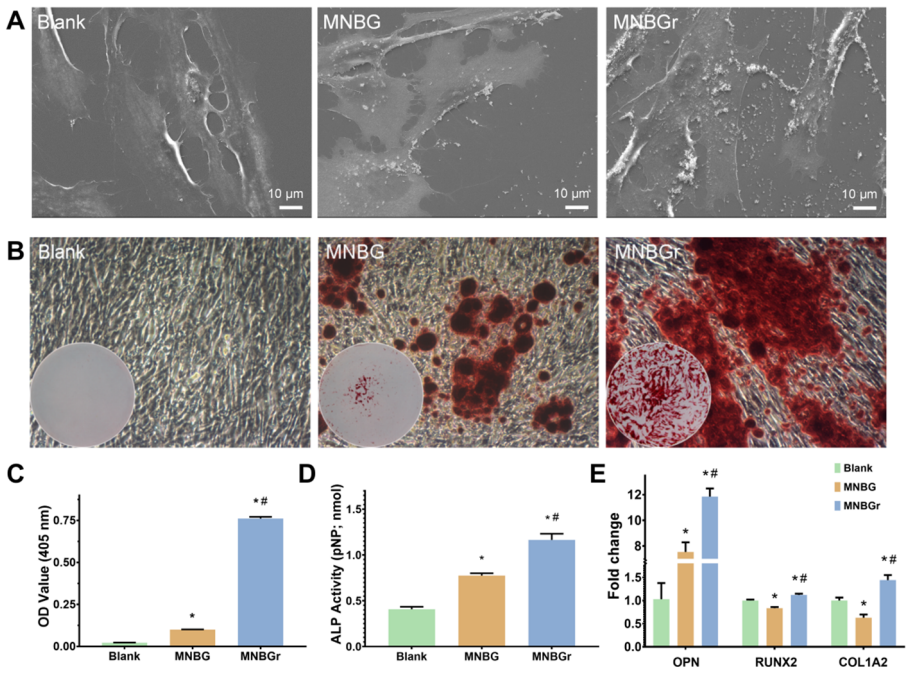

Figure 3. DPC morphology and mineralization-associated responses after exposure to MNBG or MNBGr. (**A**) SEM images after 24 h. (**B**) Representative Alizarin Red S staining after 14 days; insets show whole wells. (**C**)

Quantification of extracted Alizarin Red S at 405 nm. (**D**) ALP activity, expressed as p-nitrophenol equivalents, after 7 days. (**E**) Relative OPN, *RUNX2*, and *COL1A2* mRNA expression after 3 days. Data are presented as mean ± SD from three independent experiments. * $p < 0.05$ versus the control group; # $p < 0.05$ versus the MNBG group.

3.4. Early In Vivo Responses after Direct Pulp Capping

At 2 weeks after direct pulp capping, representative micro-CT reconstructions showed radiopaque material and mineralized tissue at the pulp-exposure sites in teeth treated with MNBG or MNBGr (Figure 4A). The MNBGr group exhibited a comparatively extensive radiopaque region, whereas less radiopaque tissue was observed in the untreated control group. Quantitative micro-CT analysis showed that bone mineral density was significantly higher in the MNBGr group than that in the control and MNBG groups (Figure 4B). Hematoxylin-eosin and Masson's trichrome staining showed a continuous, thick layer of mineralized tissue with organized collagen fibers at the exposure site in the MNBGr group (Figures 4C and 5A). In contrast, the control group exhibited incomplete mineralized tissue bridging and a less organized tissue structure. The collagen-positive area was significantly greater in both MNBG and MNBGr groups than in the control groups (Figure 5B). Immunohistochemical analysis further showed significantly higher Arg1-positive area in the MNBGr group than in the control and MNBG groups (Figure 5B), while there was no obvious change in iNOS-positive area, suggesting a shift toward a more anti-inflammatory and pro-reparative local tissue environment.

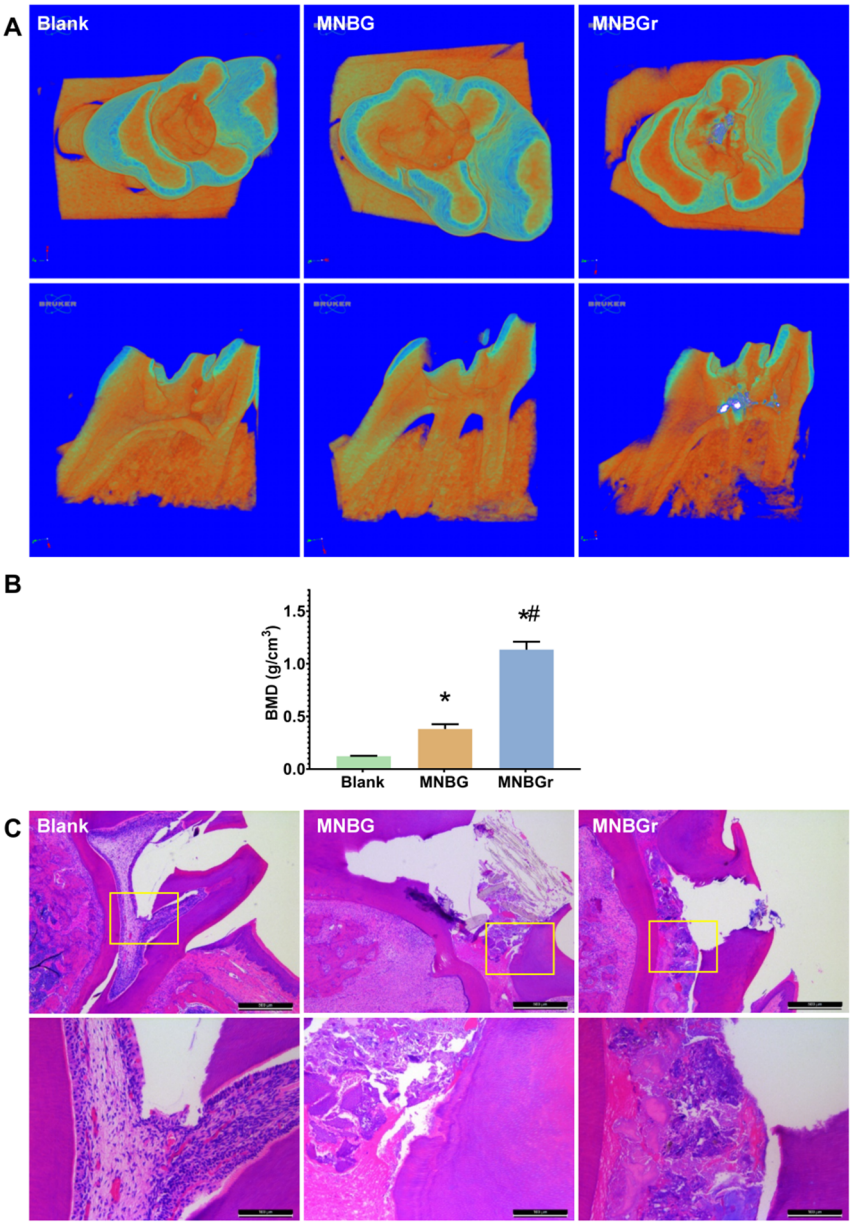

Figure 4. Early mineralized tissue formation after direct pulp capping with MNBG or MNBGr. (**A**) Representative micro-CT reconstructions at 2 weeks in occlusal and cross-sectional views. (**B**) Quantitative analysis

of bone mineral density (BMD) from the micro-CT datasets. (**C**) Representative hematoxylin-eosin-stained sections of the pulp-exposure region at 2 weeks. * $p < 0.05$ versus the control group; # $p < 0.05$ versus the MNBG group.

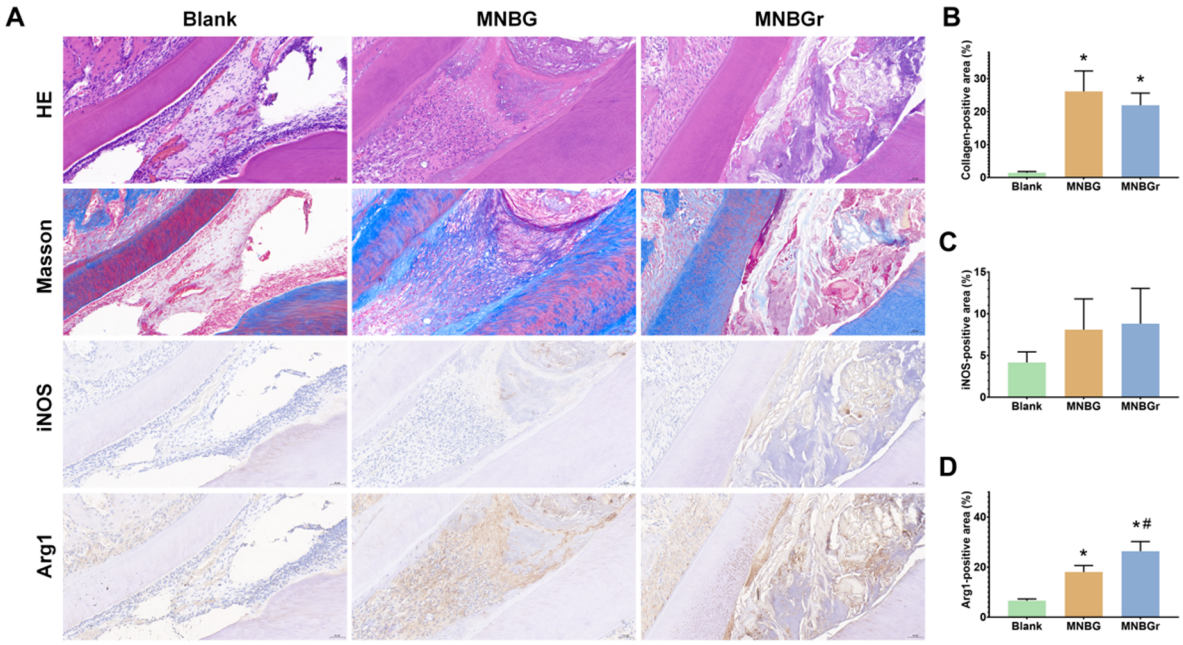

Figure 5. Histological and immunohistochemical assessment of the pulp-exposure region 2 weeks after direct pulp capping. (**A**) Representative sections showing hematoxylin-eosin staining, Masson's trichrome staining, and immunohistochemical staining for iNOS and Arg1 at ×20 magnification. (**B**–**D**) Quantification of collagen-positive area (**B**), iNOS-positive area (**C**), and Arg1-positive area (**D**). Data are presented as mean ± SD. * $p < 0.05$ versus the Blank group; # $p < 0.05$ versus the MNBG group.

4. Discussion

The extended-synthesis MNBGr formulation differed from conventional MNBG in surface architecture, particle size, and zeta potential and was associated with distinct biological responses in the dentin-pulp setting. MNBGr produced greater attenuation of LPS-induced pro-inflammatory gene expression in RAW 264.7 cells and stronger mineralization-associated responses in primary human DPCs. In the rat direct pulp-capping model, both bioactive glass formulations increased collagen deposition relative to the untreated control. Compared with MNBG, MNBGr was associated with higher bone mineral density, and higher Arg1-positive area. These findings support further investigation of the extended-synthesis formulation, although the observed biological effects cannot be attributed to surface roughness alone.

Macrophages rapidly interact with implanted biomaterials and translate physicochemical cues into inflammatory and reparative signals. In the present study, both MNBG formulations reduced LPS-induced *Il1b*, *Il6*, *Tnf*, and *Nos2* expression, with greater reductions observed for MNBGr. The concomitant increase in Arg1 staining suggests a shift toward a more pro-reparative local immune microenvironment. Biomaterial surface micro/nanostructure can regulate protein adsorption, cell adhesion, cytoskeletal organization, and phagocytic behavior [7], providing a plausible basis for the different cellular responses to MNBG and MNBGr. These findings extend previous work showing that bioactive micro/nano spheres can regulate macrophage inflammatory activity during pulp repair [11].

MNBGr also enhanced several complementary stages of the DPC mineralization response. Increased *OPN*, *RUNX2*, and *COL1A2* expression at day 3 was followed by greater ALP activity at day 7 and more extensive mineralized-matrix deposition at day 14. This temporal pattern is consistent with early activation of a mineralization-associated program and subsequent matrix maturation. The rough, flake-like surface structure may provide a larger reactive interface for ion exchange and apatite nucleation while strengthening material-cell interactions. Together with the macrophage findings, these results define a coordinated pro-reparative profile in which inflammatory regulation and DPC mineralization are complementary components of the material response [13]. Although intracellular signaling was not examined in the present study, the rough, flake-like surface of MNBGr may influence integrin-mediated adhesion and downstream FAK signaling, potentially attenuating NF-κB-driven pro-inflammatory transcription in macrophages and favoring Wnt/β-catenin-associated mineralization in DPCs [14,15]. Such topography-responsive mechanotransduction may provide a plausible link between the observed immunomodulatory

response and enhanced reparative dentin formation; however, this proposed mechanism requires direct experimental validation.

The rat direct pulp capping model provided an integrated assessment of these cellular responses within the injured dentin-pulp complex. At 2 weeks, both the MNBG- and MNBGr-treated groups exhibited greater collagen-positive area than untreated controls. Compared with MNBG, MNBGr was associated with higher bone mineral density, a more continuous mineralized tissue bridge, and higher Arg1-positive area. These findings are consistent with an early tissue healing environment that supports matrix remodeling and reparative dentin formation, indicating that extended-synthesis MNBGr may enhance early dentin-pulp complex healing.

This study has several limitations. Extending the synthesis time may concurrently alter surface morphology, particle size, and zeta potential. Moreover, surface roughness and specific surface area were not quantified, and size-matched controls were not included. Therefore, the present comparison cannot identify surface roughness as the sole determinant of the observed biological responses. The *in vivo* analysis was also limited by a small sample size and a single 2-week time point. In addition, odontoblast-specific markers such as DSPP and DMP1 were not examined. Future studies should quantify surface roughness, specific surface area, porosity, and ion-release kinetics; incorporate size-matched controls, larger sample sizes, and longer observation periods; and include odontoblast-specific markers to characterize the reparative response more precisely.

5. Conclusions

Micro/nano bioactive glass spheres produced by extended synthesis attenuated pro-inflammatory gene expression in RAW 264.7 cells, enhanced mineralization-associated responses in primary human DPCs, and supported early reparative tissue formation in a rat direct pulp-capping model. These findings support the further investigation of MNBGr as a potential material for vital pulp therapy. However, because extended synthesis concurrently altered several physicochemical properties, the observed biological effects cannot be attributed to surface roughness alone.

Author Contributions

Z.L.: conceptualization, investigation, data curation, writing—original draft preparation; T.W.: visualization, investigation; Y.X.: supervision; Y.Z.: conceptualization, supervision, writing—reviewing and editing. All authors have read and agreed to the published version of the manuscript.

Funding

This work was supported by the National Natural Science Foundation of China (NSFC) General Project (Grant No. 31771025), the Guangzhou Science and Technology Projects (202201020396), and Technology Innovation Group Project of Foshan (FS0AA-KJ919-4402-0027).

Institutional Review Board Statement

The study was conducted in accordance with the Declaration of Helsinki, and approved by the Human Research Ethics Committee of the Affiliated Stomatology Hospital of Guangzhou Medical University (approval no. JCYJ2024004, granted on 19 June 2024). All animal procedures were approved by the Animal Ethics Committee of Guangzhou Medical University (approval no. 20191115006, granted on 15 November 2019).

Informed Consent Statement

Not applicable.

Data Availability Statement

The data supporting the findings of this study are available from the corresponding author upon reasonable request.

Conflicts of Interest

Tao Wang is affiliated with GemPharmatech Co., Ltd., Guangzhou, China, and declares no conflict of interest. Given the role as Editor, Yin Xiao had no involvement in the peer review of this paper and had no access to information regarding its peer-review process. Full responsibility for the editorial process of this paper was delegated to another editor of the journal. The remaining authors declare no conflict of interest.

Use of AI and AI-Assisted Technologies

During the preparation of this work, the authors used DeepSeek to improve the language and readability of the manuscript. All outputs were reviewed and edited by the authors, who take full responsibility for the content of the publication.

References

1. Pitts, N.B.; Zero, D.T.; Marsh, P.D.; et al. Dental caries. *Nat. Rev. Dis. Prim.* **2017**, *3*, 17030. https://doi.org/10.1038/nrdp.2017.30.
2. Hamilton, A.R.; Ricketts, D. Management of deep caries. *Br. Dent. J.* **2026**, *240*, 357–364. https://doi.org/10.1038/s41415-025-9350-7.
3. Cooper, P.R.; Friedlander, L.T.; Hussaini, H.M.; et al. Inflammation and Regeneration in the Dentine-Pulp Complex: Where Are We Now and Where Are We Going? *J. Endod.* **2026**, *52*, 1927–1933. https://doi.org/10.1016/j.joen.2026.08.019.
4. Tian, T.; Xie, W.; Gao, W.; et al. Micro-Nano Bioactive Glass Particles Incorporated Porous Scaffold for Promoting Osteogenesis and Angiogenesis *in vitro*. *Front. Chem.* **2019**, *7*, 186. https://doi.org/10.3389/fchem.2019.00186. Correction in *Front. Chem.* **2022**, *10*, 891108.
5. Zhou, Y.; Han, S.; Xiao, L.; et al. Accelerated host angiogenesis and immune responses by ion release from mesoporous bioactive glass. *J. Mater. Chem. B* **2018**, *6*, 3274–3284. https://doi.org/10.1039/c8tb00683k.
6. Zhou, Y.; Shi, M.; Jones, J.R.; et al. Strategies to direct vascularisation using mesoporous bioactive glass-based biomaterials for bone regeneration. *Int. Mater. Rev.* **2017**, *62*, 392–414. https://doi.org/10.1080/09506608.2016.1266744.
7. Xu, T.; Xie, K.; Wang, C.; et al. Immunomodulatory nanotherapeutic approaches for periodontal tissue regeneration. *Nanoscale* **2023**, *15*, 5992–6008. https://doi.org/10.1039/d2nr06149j.
8. Luo, J.; Walker, M.; Xiao, Y.; et al. The influence of nanotopography on cell behaviour through interactions with the extracellular matrix—A review. *Bioact. Mater.* **2022**, *15*, 145–159. https://doi.org/10.1016/j.bioactmat.2021.11.024.
9. Zhou, Y.; Xu, T.; Han, P.; et al. Biological Responses to Biomaterials: Mechanisms and Opportunities for Enhanced Oral Tissue Regeneration. *J. Periodontal Res.* **2026**. https://doi.org/10.1111/jre.70078.
10. Zhou, Y.; Xu, T.; Wang, C.; et al. Clinical usage of dental stem cells and their derived extracellular vesicles. In *Progress in Molecular Biology and Translational Science*; Elsevier: Amsterdam, The Netherlands, 2023; Volume 199, pp. 297–326. https://doi.org/10.1016/bs.pmbts.2023.03.005.
11. Li, Z.; Xie, K.; Yang, S.; et al. Multifunctional Ca–Zn–Si-based micro-nano spheres with anti-infective, anti-inflammatory, and dentin regenerative properties for pulp capping application. *J. Mater. Chem. B* **2021**, *9*, 8289–8299. https://doi.org/10.1039/d1tb01517f.
12. Ellerbrock, R.; Stein, M.; Schaller, J. Comparing amorphous silica, short-range-ordered silicates and silicic acid species by FTIR. *Sci. Rep.* **2022**, *12*, 11708. https://doi.org/10.1038/s41598-022-15882-4.
13. Yang, F.; Hou, J.; Dargaville, T.R.; et al. Advances in peptide applications for hard tissue repair and regeneration: Multidisciplinary perspectives. *Chem. Soc. Rev.* **2026**, *55*, 9209–9294. https://doi.org/10.1039/d4cs01211a.
14. Zheng, X.; Wang, S.; Xiao, L.; et al. LiCl -induced immunomodulatory periodontal regeneration via the activation of the Wnt/β-catenin signaling pathway. *J. Periodontal Res.* **2022**, *57*, 835–848. https://doi.org/10.1111/jre.13022.
15. Shin, J.J.; Park, J.; Shin, H.S.; et al. Roles of lncRNAs in NF-κB-Mediated Macrophage Inflammation and Their Implications in the Pathogenesis of Human Diseases. *Int. J. Mol. Sci.* **2024**, *25*, 2670. https://doi.org/10.3390/ijms25052670.